

Vector tomography applications in plasma diagnostics

John Howard

Plasma Research Laboratory, Research School of Physical Sciences and Engineering, Australian National University, Canberra, 0200 Australia

Received 18 May 1995, in final form 30 October 1995

Abstract. The application of tomographic techniques for the study of vector fields has been demonstrated only in the last few years. We show its potential for remote sensing of plasma vector fields such as the fluid velocity v and the magnetic field B using Doppler and Zeeman spectroscopy. Simulations suggest the possibility of time-resolved reconstruction of ion velocity flow fields and poloidal magnetic fields from direct measurements of the low-order spectral moments of line-integrated spectroscopic measurements. Other possible applications of vector tomography are examined.

1. Introduction

Despite its long history, application of tomography to other than scalar fields has only been exploited recently. For example, work in ultrasonic imaging of fluid flows has clearly illustrated the power of vector methods for reconstruction of fluid vorticity from differential ultrasonic time-of-flight measurements [25]. The method applies to line-integral measurement of either the component of the vector field parallel (longitudinal) or transverse to the direction of integration. The vector component measurements can be related to the line-integral of associated scalar quantities which then yield to standard tomography methods.

There are a number of possible applications for vector tomography in plasma diagnostics. For example, Balandin [1] has proposed vector tomography of laser Faraday rotation measurements, the laser polarization responding to the component of the magnetic field parallel to the beam with the ellipticity being sensitive to the transverse component.

In this paper, we focus on the application of vector tomography methods to standard Doppler spectroscopy (which is sensitive to the component of the bulk ion velocity in the viewing direction) and Zeeman effect polarimetry that registers the poloidal magnetic field component along the line-of-sight. Up until now, charge-exchange recombination spectroscopy [11] and beam emission spectroscopy [10] have proved very successful in sensing bulk plasma motions. Both the Zeeman effect from an injected Lithium beam [15] and the motional Stark effect from hydrogenic neutral beams [27] have been used for local magnetic field measurements. However, such methods rely on the presence or availability of neutral heating or diagnostic beams and the region over which information is obtained is limited accordingly. In principle, passive spectroscopy suffers neither of these drawbacks. The zeroth-order spectral moment of the emission line gives the line-integrated emissivity or brightness. This can be inverted using scalar tomography. Though the emission tends to be confined to toroidal shells having electron temperature comparable with the excitation potential, the radial emission profile for transitions in more highly-ionized ions can also be quite broad [26]. The first moment gives the emission-weighted

Doppler shift in the observation direction and, as will be demonstrated, is amenable to methods of vector tomography. The second spectral moment is, of course, related to the ionic temperature and again yields to scalar techniques.

The paper is organized as follows. The basic results for the line-integral transform of three-dimensional vector fields are expounded using the theorems of Stokes and Gauss (section 1). This approach is intuitive and extends naturally to the Radon transform in three dimensions. For two-dimensional fields or cylindrical symmetry (subsection 2.1), the results reduce to those obtained by Braun and Hauck [5]. The cylindrical idealization is closely approximated in toroidal plasma confinement devices where the scale length for variations in the poloidal cross section is usually much less than in the toroidal (z) direction.

Applications in spectroscopy are discussed in sections 3 and 4. We suggest measurement schemes for simultaneous detection of all three low-order spectral moments of the emission line. Specifically, we propose to exploit the natural spectral weighting of a Fourier transform spectrometer to optically compute the moments for optimum signal-to-noise ratio and maximum time response.

Other applications in plasma diagnostics are discussed in section 5 and results of numerical simulations presented in section 6. In particular, we examine the feasibility of spectroscopic vector imaging of flow fields in the H-1 heliac, a helical axis stellarator at the ANU [12].

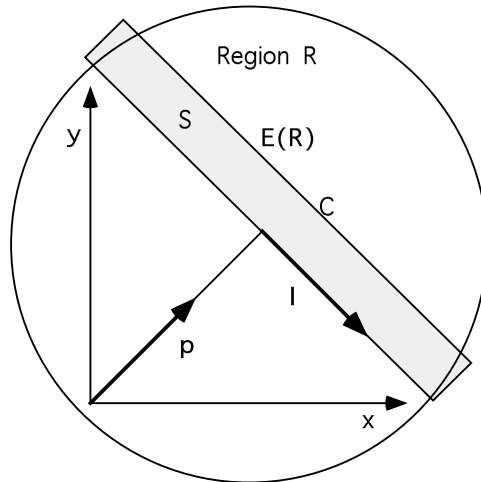


Figure 1. Diagram showing the geometry for tomography of vector fields. The line-of-sight is parallel to the direction \hat{l} . Stokes theorem is applied to the vector field $E(\mathbf{R})$ and evaluated over surface area S in the x - y plane bounded by the closed path C . The vector field is assumed to vanish outside the region R .

2. Vector tomography

For a general vector field $E(\mathbf{R}) = E_x(\mathbf{R})\hat{i} + E_y(\mathbf{R})\hat{j} + E_z(\mathbf{R})\hat{k}$, where $\mathbf{R} = (x, y, z)$ is a position vector, Stokes theorem can be written in the familiar form

$$\oint_C \mathbf{E} \cdot d\mathbf{l} = \int_S (\nabla \times \mathbf{E}) \cdot d\mathbf{s} \quad (1)$$

where S is the surface enclosed by the path C , $d\mathbf{l} = \hat{\mathbf{l}} dl$ and $d\mathbf{s} = \hat{\mathbf{k}} ds$ are line and surface elements and $\hat{\mathbf{l}} = (-\sin\phi, \cos\phi)$ and $\hat{\mathbf{k}}$ are unit vectors. We take the measurement region R to be bounded and contained in the x - y plane and integrate the vector field over the narrow rectangular path C as shown in figure 1. The vector fields of interest in this article can be written as the product of a scalar field (which vanishes at the plasma periphery) and a vector field such as the plasma velocity \mathbf{v} or magnetic field \mathbf{B} . The Faraday rotation of the plane of polarization of a far-infrared laser beam, for example, is sensitive to the product of the electron density distribution n_e and the magnetic field \mathbf{B} . As a result, we can neglect contributions to the closed path integral in equation (1) from regions outside the plasma. With definitions

$$G_l = \int_{L_1}^{L_2} E_l dl \quad (2)$$

and

$$\begin{aligned} E_l &= -\sin\phi E_x + \cos\phi E_y = \hat{\mathbf{l}} \cdot \mathbf{E} \\ E_p &= \cos\phi E_x + \sin\phi E_y = \hat{\mathbf{p}} \cdot \mathbf{E} \end{aligned}$$

where p is the coordinate in the direction ϕ (see figure 1) and L_1 and L_2 lie on the boundary of R , equation (1) can be expressed as

$$\int_{L_1}^{L_2} [E_l(p + \Delta p) - E_l(p)] dl = - \int_{L_1}^{L_2} \int_p^{p+\Delta p} (\nabla \times \mathbf{E})_z dl dp. \quad (3)$$

In the limit $\Delta p \rightarrow 0$ this gives

$$\int_{L_1}^{L_2} \frac{\partial E_l}{\partial p} dl = - \int_{L_1}^{L_2} \Omega_z dl \quad (4)$$

where $\Omega = \nabla \times \mathbf{E}$ is the vorticity. In general, the endpoints L_1 and L_2 can be functions of p so that the left-hand side of equation (4) is written

$$\int_{L_1}^{L_2} \frac{\partial E_l}{\partial p} dl - \frac{\partial L_1}{\partial p} E_l(L_1, p) + \frac{\partial L_2}{\partial p} E_l(L_2, p) = \frac{\partial G_l}{\partial p}. \quad (5)$$

The result is that the measurement of the transverse gradient of the line-integrated ‘longitudinal’ component of the vector field G_l can be related to the *scalar* line integral of the z -component of the vorticity. The scalar problem then yields to standard tomographic procedures. Indeed, upon Fourier transformation with respect to p , equation (4) gives a ‘projection slice theorem’ for Ω_z [25]. Using a tilde to denote reciprocal space quantities, the result is

$$-i\kappa \tilde{G}_l(\kappa, \phi) = \tilde{\Omega}_z(\kappa) \quad (6)$$

where $\kappa = \kappa(\cos\phi, \sin\phi)$ is the reciprocal space coordinate and the z -dependence is understood.

The line integral of the vector component of \mathbf{E} transverse to the line-of-sight is conveniently treated using an alternative form of Stokes theorem:

$$\oint_C \mathbf{E} \times d\mathbf{l} = \int_S (d\mathbf{s} \times \nabla) \times \mathbf{E}. \quad (7)$$

Evaluating this integral around the closed loop C and taking the limit $\Delta p \rightarrow 0$, gives for the z -component

$$\frac{\partial G_p}{\partial p} = - \int_{L(p, \phi)} \nabla_T \cdot \mathbf{E}_T dl \quad (8)$$

where $L(p, \phi)$ denotes the line of integration, $\mathbf{E}_T = (E_x, E_y)$, ∇_T is the gradient operator in the x - y plane and we have defined the ‘transverse’ line integral

$$G_p = \int_{L(p, \phi)} E_p \, dl. \quad (9)$$

Introducing the ‘source’ function $\rho_T = \nabla_T \cdot \mathbf{E}_T$ and taking the Fourier transform with respect to impact parameter p results in a slice theorem for the transverse measurement that is analogous to equation (6):

$$-i\kappa \tilde{G}_p(\kappa, \phi) = \tilde{\rho}_T(\kappa). \quad (10)$$

2.1. Cylindrical vector fields

It will be noted that equation (4) involves taking the derivative of the measured quantities for reconstruction of the z -component of the vorticity, itself related by differentiation to the field \mathbf{E} . The same is true for transverse measurements. A relationship between the measurements and the more primitive vector and scalar potentials of \mathbf{E} can be derived using the Helmholtz theorem (see [19, 5]). The theorem decomposes \mathbf{E} into the sum of its irrotational and solenoidal parts:

$$\begin{aligned} \mathbf{E} &= \mathbf{E}_V + \mathbf{E}_W \\ &= -\nabla V + \nabla \times \mathbf{W} \end{aligned} \quad (11)$$

where $\mathbf{W}(\mathbf{r})$ and $V(\mathbf{r})$ are respectively vector and scalar potentials. When the field considered is bounded, it is appropriate to introduce a third harmonic vector field \mathbf{E}_H that satisfies certain boundary conditions. We then write

$$\mathbf{E} = \mathbf{E}_{V0} + \mathbf{E}_{W0} + \mathbf{E}_H \quad (12)$$

where \mathbf{E}_{V0} and \mathbf{E}_{W0} are homogeneous in the sense that the normal component of \mathbf{E}_{W0} and the tangential component of \mathbf{E}_{V0} vanish at the boundary of R . The homogeneity condition implies that the potential fields V_0 and W_0 associated with \mathbf{E}_{V0} and \mathbf{E}_{W0} are constant on the boundary. The component \mathbf{E}_H , which then fulfills the boundary conditions, is both irrotational and solenoidal and can be described in terms of a scalar potential function that satisfies the Laplace equation. Since the vector fields of interest here vanish beyond the boundary it is not necessary to consider further the boundary harmonic field (but see [5, 2]).

Now note that

$$\boldsymbol{\Omega} = \nabla \times \mathbf{E} = \nabla \times \mathbf{E}_W = -\nabla^2 \mathbf{W} \quad (13)$$

$$\rho = \nabla \cdot \mathbf{E} = \nabla \cdot \mathbf{E}_V = -\nabla^2 V \quad (14)$$

where \mathbf{W} is chosen so that the term $\nabla \cdot \mathbf{W}$ in the expansion of $\nabla \times \nabla \times \mathbf{W}$ vanishes. This choice of gauge requires that the component of \mathbf{W} normal to the boundary be zero [2]. For the quantities that can be retrieved from measurements in a plane, we have

$$\Omega_z = -\nabla^2 W_z \quad (15)$$

$$\rho_T = \rho + \frac{\partial^2 V}{\partial z^2} \quad (16)$$

and it is clear that the associated potentials W_z and V can be recovered only when their z -variation vanishes. We thus define a cylindrical field as one for which the z -variation of all potential components (W_x, W_y, W_z) and V vanishes. Fourier transformation of

equations (15) and (16) and substitution into equations (6) and (10) gives projection slice theorems for the cylindrical vector and scalar potentials

$$\tilde{G}_l(\kappa, \phi) = i\kappa \tilde{W}_z(\kappa) \quad (17)$$

$$\tilde{G}_p(\kappa, \phi) = i\kappa \tilde{V}(\kappa). \quad (18)$$

Observe that the zeroth moments of G_l and G_p are zero. This can provide a useful cross-check on the assumed homogeneity of \mathbf{E} in experimental situations. The potentials can be recovered from the measurements using the inversion formulae obtained in the appendix. For cylindrical fields, longitudinal vector field measurements in the poloidal x - y plane are then sufficient for determination of the solenoidal field $\mathbf{E}_W = \nabla \times W_z \hat{\mathbf{k}}$. Indeed, taking the Fourier transformation of (11) and using the results from equations (17) and (18) gives a slice theorem for the vector field

$$\tilde{\mathbf{E}}(\kappa) = \tilde{G}_p(\kappa) \hat{\mathbf{p}} + \tilde{G}_l(\kappa) \hat{\mathbf{l}}. \quad (19)$$

2.2. Extension to planar integrals

By analogy with the development using Stokes theorem, the Radon transform of vector fields in three dimensions (planar integrals) can be conveniently handled using the two forms of the Gauss integral vector theorem

$$\int_S \mathbf{E} \cdot d\mathbf{s} = \int_V \nabla \cdot \mathbf{E} dV \quad (20)$$

$$\int_S d\mathbf{s} \times \mathbf{E} = \int_V \nabla \times \mathbf{E} dV \quad (21)$$

where $d\mathbf{s}$ is the element of area, $dV = dx dy dz$ and V is the volume enclosed by the surface S . By analogy with the two-dimensional case, we consider a box-like volume and allow the volume to become infinitesimally narrow in the direction $\hat{\mathbf{p}}$ of the normal to the planes of integration. Providing the edge contributions vanish we obtain

$$\frac{\partial G_p}{\partial p} = \int_{A(p,\phi)} \nabla \cdot \mathbf{E} ds \quad (22)$$

$$\frac{\partial G_l}{\partial p} = - \int_{A(p,\phi)} (\nabla \times \mathbf{E}) \cdot \hat{\mathbf{m}} ds \quad (23)$$

where

$$G_p = \int_{A(p,\phi)} \mathbf{E} \cdot \hat{\mathbf{p}} ds \quad (24)$$

$$G_l = \int_{A(p,\phi)} \mathbf{E} \cdot \hat{\mathbf{l}} ds \quad (25)$$

$A(p, \phi)$ designates the plane of integration, and the unit vectors $(\hat{\mathbf{l}}, \hat{\mathbf{m}}, \hat{\mathbf{p}})$ form a right-handed system. In contrast with line-integral measurements in a plane, the solenoidal and irrotational parts of the three-dimensional field are fully determined by sufficient planar integral measurements. Though central section theorems can be developed analogous to the two-dimensional case, our interest here is in line-integrals and we pursue the planar case no further.

3. Doppler spectroscopy

Spectroscopic measurements of the line radiation emitted from atomic or ionic species in a magnetized high-temperature plasma is a standard diagnostic technique. Though we shall refer to ionic emission below, similar considerations apply for atoms. We assume the emission is locally isotropic and to be measured in a planar plasma cross section along well-defined lines-of-sight. Ignoring all but Doppler broadening mechanisms, the local power per unit volume (the emissivity) at frequency ν and position $\mathbf{r} = (x, y)$ in the plasma and in the direction $\hat{\mathbf{l}}$ is given by a velocity-space line integral over the ion velocity distribution function f [22]

$$I(\mathbf{r}, \hat{\mathbf{l}}; w) = I_0(\mathbf{r}) \int_{-\infty}^{\infty} f(\boldsymbol{\beta}) \delta(w - \boldsymbol{\beta} \cdot \hat{\mathbf{l}}) d\boldsymbol{\beta} \quad (26)$$

where $\boldsymbol{\beta}(\mathbf{r}) = \mathbf{v}(\mathbf{r})/c$ is the vector velocity field, $d\boldsymbol{\beta} = dv_x dv_y/c^2$, $w = (\nu - \nu_0)/\nu_0$ is a normalized frequency coordinate and ν_0 is the emission line centre. The \mathbf{r} -dependence of f is absorbed by the spectrally integrated local intensity $I_0(\mathbf{r})$.

It is clear that the central frequency moments of I are proportional to the velocity moments of the distribution function in the direction $\hat{\mathbf{l}}$. From sampling considerations, it can be shown that M angularly equispaced projections (a projection is the set of all line integrals in a given direction) of an arbitrary source distribution f determine $M^2 + M$ moments of f , free of angular aliasing contamination from higher-order terms [13]. These moments are proportional to the corresponding moments of the projection set. Thus, for example, the spectrum of radiation emitted along the x -axis gives the value of $f(\beta_x, \beta_y)$ integrated over β_y . From such a single projection can be recovered unambiguously the zeroth moment of f (here normalized to unity) and the centre-of-mass of the velocity distribution in the direction β_x . Measurement of the radiation in two different directions should, therefore, unambiguously determine the mean drift velocity vector for the group of emitters at \mathbf{r} .

For an extended medium we must sum the intensities over the emitting elements along the line-of-sight. Is it possible to unfold the structure of the emitter flow field from such spatially integrated measurements? Assuming that the transition is optically thin and that the optical system is well collimated, the spectroscopic measurement can be regarded as an ideal line integral of the emission over the line $L(p, \phi)$:

$$\begin{aligned} g(p, \phi; w) &= \int_{-\infty}^{\infty} d\mathbf{r} I_0(\mathbf{r}) \delta(p - \mathbf{r} \cdot \hat{\mathbf{p}}) \int_{-\infty}^{\infty} d\boldsymbol{\beta} f(\boldsymbol{\beta}) \delta(w - \boldsymbol{\beta} \cdot \hat{\mathbf{l}}) \\ &\equiv \int_{L(p, \phi)} I(\mathbf{r}, \hat{\mathbf{l}}; w) dl \end{aligned} \quad (27)$$

where $d\mathbf{r} = dx dy$ and the integration over solid angle gives a constant factor that is absorbed by I_0 . For concreteness, we consider the usual case of an isotropic Maxwellian ion velocity distribution shifted by the gross flow $\boldsymbol{\beta}_D(\mathbf{r}) = \mathbf{v}_D(\mathbf{r})/c$. The local spectrum is the Gaussian emission profile

$$I(\mathbf{r}, \hat{\mathbf{l}}; w) = \frac{I_0(\mathbf{r})}{\sqrt{2\pi}\sigma(\mathbf{r})} \exp[-(w - \beta_D)^2/2\sigma^2(\mathbf{r})] \quad (28)$$

where $\beta_D = \boldsymbol{\beta}_D \cdot \hat{\mathbf{l}}$ is the normalized Doppler frequency shift of the spectral line and the line broadening $\sigma(\mathbf{r})$ is related to the ionic temperature T and weight m_a by $\sigma^2(\mathbf{r}) = kT(\mathbf{r})/m_a c^2$ [16]. The possibility of Zeeman effect broadening is also considered below.

It is often the case that the radiation from a given ionic transition is spatially localized to a narrow toroidal shell. The radiation is usually spectrally resolved and a best-fit Gaussian computed to estimate the emission intensity, Doppler shift and ionic temperature. In general, however, the spectral distribution of the emission, being the integral of shifted Gaussians, is itself not Gaussian (see for example [22]). Nevertheless, the important information can be obtained directly and precisely from the low-order spectral moments of the line-integrated emission. Defining the spectral moments by

$$\mu^{(m)} = \int_{-\infty}^{\infty} g(p, \phi; w) w^m dw \quad (29)$$

it is straightforward to show that

$$\mu^{(0)} = \int_{L(p, \phi)} I_0(\mathbf{r}) dl \quad (30)$$

$$\mu_D^{(1)} = \int_{L(p, \phi)} I_0(\mathbf{r}) \beta_D(\mathbf{r}) \cdot dl \quad (31)$$

and

$$\mu_D^{(2)} = \int_{L(p, \phi)} I_0(\mathbf{r}) [\sigma^2(\mathbf{r}) + \beta_D^2(\mathbf{r})] dl. \quad (32)$$

Note that equation (31) is valid for any spectral profile of even symmetry.

For measurements sufficiently covering the space (p, ϕ) , the intensity distribution can be inferred approximately by applying standard tomographic methods to invert equation (30) [20, 17]. However, using earlier developed principles of longitudinal vector tomography, it should be equally plausible to recover the solenoidal part of the intensity-weighted bulk ion flow from measurements of $\mu^{(1)}$ and estimates of the species temperature distribution from $\mu_D^{(2)}$. Higher-order moments convey additional information about the spatial distribution of the emission parameters and could be used to further constrain the reconstruction.

It is desirable to relate the measurement of W_z to properties of the underlying vector field \mathbf{v} . For this purpose we transform equation (11) to the form

$$\mathbf{E} = -\nabla V + \nabla \times \mathbf{W} = -I_0 \nabla v + I_0 \nabla \times \mathbf{w} \quad (33)$$

where v and \mathbf{w} are the potentials describing the velocity field \mathbf{v} . Equation (33) can be rearranged as

$$\mathbf{H} = \nabla V - I_0 \nabla v = \nabla \times \mathbf{W} - I_0 \nabla \times \mathbf{w}. \quad (34)$$

Provided the fields $I_0 \nabla v$ and $I_0 \nabla \times \mathbf{w}$ are, respectively, irrotational and solenoidal, that is, when

$$\nabla I_0 \times \nabla v = 0 \quad \text{and} \quad \nabla I_0 \cdot \nabla \times \mathbf{w} = 0 \quad (35)$$

the field \mathbf{H} is both irrotational and solenoidal and can be written as the gradient of a scalar potential that satisfies Laplace's equation. Since \mathbf{H} vanishes at the boundary, the potential must be constant there and, because it is harmonic, must therefore be constant everywhere inside the region R . Thus, under the conditions (35), we have $\mathbf{H} = 0$ and longitudinal or transverse measurements are able to distinguish the corresponding solenoidal or irrotational components of the underlying field \mathbf{v} , respectively.

3.1. Measurement schemes

The three spectral moments can be measured experimentally by exploiting the frequency response $W(\nu)$ of the dispersing instrument. As a simple example, a grating spectrometer having input and output slits of equal width will exhibit a triangular instrument response. The signal obtained by tuning the instrument so that the nominal spectral line centre ν_0 is in the rise or fall of the profile will be responsive to changes in both $\mu^{(0)}$ and $\mu_D^{(1)}$. Simultaneous measurements in adjacent spectral channels either side of ν_c will then suffice to determine the two lowest-order moments.

An alternative scheme may be constructed using interference filters. A first broadband filter isolates the spectral line of interest. This is followed by a second narrowband filter tilted in such a way that the spectral line centre falls in the wings of the passband where the transmission is assumed to decrease in a linear fashion. The transmitted and reflected beams are then sufficient for determination of $\mu^{(0)}$ and $\mu_D^{(1)}$. With the insertion of an additional filter it would be possible to measure uniquely the three low-order moments of the emission line. One difficulty with this method is to ensure that the filter gradient is sufficiently steep to give accurately measurable difference signals.

One means to control and/or increase the sensitivity to the first moment is to use a Fourier transform spectrometer [3]. As for the filters, the interferometer offers a significant increase in optical throughput over grating spectrometers (the Jacquinot advantage) and can be adapted easily for multiple spatial channels. The intensity at the interferometer output port is proportional to

$$S = \int_0^\infty g[p, \phi; (\nu - \nu_0)/\nu_0][1 + \cos(2\pi\nu\Delta/c)] d\nu \quad (36)$$

where Δ/c is the time delay due to the path length difference Δ . Substituting from equations (27) and (28) gives

$$S = \mu^{(0)} + \int_{L(p, \phi)} I_0(\mathbf{r}) \cos[\varphi(1 + \beta_D(\mathbf{r}))] \exp[-\sigma^2(\mathbf{r})\varphi^2/2] d\mathbf{l} \quad (37)$$

where $\varphi = 2\pi\nu_0\Delta/c$. The kernel nonlinearity can be exploited using modulation techniques to generate the required spectral moments of the integrated emission. The modulation can be achieved by vibrating one of the mirrors of the Michelson configuration with small amplitude φ_1 about some dc position φ_0 to give an instantaneous phase delay

$$\varphi = \varphi_0 + \varphi_1 \sin \Omega t. \quad (38)$$

For $\varphi_0 = (2n + 1)\pi/2$, the lowest harmonic components of the interferometric signal are

$$\tilde{S} = \mu^{(0)} + J_0(\varphi_1)\varphi_0\mu_D^{(1)} + J_1(\varphi_1)\varphi_0^2\mu_D^{(2)} \sin \Omega t + 2J_2(\varphi_1)\varphi_0\mu_D^{(1)} \cos 2\Omega t \quad (39)$$

where we have retained only lowest-order terms in the small quantities $\beta_D\varphi_0$ and $\sigma\varphi_0$. Sensitivity to the moments can be adjusted through the offset φ_0 . The maximum offset is ultimately limited by the coherence length of the light, this depending on the temperature of the source. The dc sensitivity to the first moment can be tuned out by choosing the modulation depth φ_1 equal to one of the zeros of J_0 . The temporal resolution of the scheme is of course fixed by the modulation frequency. Higher harmonics give information about the higher moments of the emission radiation.

Using the spectrometer to optically compute the low-order moments eliminates the need for multi-element CCD arrays usually required to resolve the emission line. This should allow a significant increase in time-resolution (by having no longer to await the array read-out) and should enhance the signal-to-noise ratio by allowing the use of instruments of high étendue.

4. Zeeman spectroscopy

The measurement of the poloidal magnetic field in a tokamak from the Zeeman splitting and polarization of the magnetic dipole radiation from heavy ions was suggested by Feldman [9]. This was followed by experiments that successfully demonstrated the feasibility of such measurements on the TEXT tokamak by Wroblewski *et al* [28, 26]. While the results were promising, the accuracy of the method was limited by signal-to-noise ratio problems. More recently, however, accurate measurements of the poloidal field profile in the outer region of JIPP T-IIU discharges during current ramping experiments have been obtained by measuring the Zeeman splitting of HeII (468.8 nm) [18]. Zeeman absorption of resonant radiation from a tunable laser [23] could also alleviate signal-to-noise ratio difficulties, but plasma access is a limitation. Methods suggested in the previous section, that make use of the radiation across the full line profile, adapt easily to both Zeeman emission and absorption measurements and could give improved signal-to-noise ratio. Though a thorough discussion of the principle of Zeeman effect measurements is given by Feldman, for clarity, we summarize here the basic elements of the technique.

The upper and lower levels of an atom in a weak magnetic field are split into $2J + 1$ sublevels with energy shifts given by

$$\Delta E_{JM} = g_{\alpha JM} M \mu B \quad (40)$$

where, for L - S coupling, $g_{\alpha JM}$ is the Landé splitting factor, μ is the Bohr magneton and α denotes quantum numbers other than the total angular momentum J and magnetic quantum number $|M| \leq J$. Because of these shifts, the spectral line is split into a number of components whose relative intensities and polarizations depend on the corresponding changes in J and M [9, 6]. Viewed in the direction of B , the intensity is zero for the $\Delta M = 0$ lines and is circularly polarized clockwise for $\Delta M = +1$ and counterclockwise for $\Delta M = -1$. Viewed in the direction perpendicular to B , the emission is linearly polarized perpendicular to B for $\Delta M = 0$ and parallel to B for $\Delta M = \pm 1$. For tokamaks, this splitting is often small compared with the Doppler broadening. The polarization tagging of the frequency shifted Zeeman components is thus essential for their discrimination against the unshifted component.

When measuring the emission in a poloidal plane, the angle $\gamma(\mathbf{r})$ between the helical field lines and the line-of-sight depends on the local poloidal component of the field. This determines the polarization properties of the radiation emitted in the direction $\hat{\mathbf{l}}$. The local radiant intensity for the n th spectrally-shifted circular component is $\epsilon_n^{(\Delta M)} I(\mathbf{r}, \hat{\mathbf{l}}; w + w_n^{(\Delta M)})$ where I is the intensity of the unperturbed line (cf equation (26)) and $\epsilon_n^{(\Delta M)}$ is the relative intensity and $w_n^{(\Delta M)}$ the normalized frequency shift of the n th line of the group exhibiting the change in magnetic quantum number ΔM . The resulting spectrum and polarization state of the emergent radiation is the integral over the line-of-sight of the contributions from all components of the Zeeman multiplet.

To measure the net circular polarization, a phase plate having delay δ and polarization analyser (with their axes at 45°) can be inserted into the beam. Following Feldman [9], the resulting intensity of the line radiation transmitted through the polarizing components (assuming there is a prefilter to isolate the Zeeman pattern from the background) can be calculated as

$$g(p, \phi; w) = 2 \int_{L(p, \phi)} d\mathbf{l} \left\{ [\cos^2(\delta/2) \cos^2 \gamma(\mathbf{r})] \sum_{n=0}^{2J+1} \epsilon_n^{(0)} I(\mathbf{r}, \hat{\mathbf{l}}, w + w_n^{(0)}) \right.$$

$$\begin{aligned}
& +[\sin(\delta/2) + \cos(\delta/2) \sin \gamma(\mathbf{r})]^2 \sum_{n=0}^{2J+1} \epsilon_n^{(1)} I(\mathbf{r}, \hat{\mathbf{l}}, w + w_n^{(1)}) \\
& +[\sin(\delta/2) - \cos(\delta/2) \sin \gamma(\mathbf{r})]^2 \sum_{n=0}^{2J+1} \epsilon_n^{(-1)} I(\mathbf{r}, \hat{\mathbf{l}}, w + w_n^{(-1)}) \}. \quad (41)
\end{aligned}$$

The frequency shifts and rules for the relative intensities are described in many texts (for example, [6]). Of importance here is that, for weak fields, the Zeeman multiplet is symmetric about the undisplaced line $w_n^{(-1)} = -w_n^{(+1)}$ and that the intensity sum for all lines originating (ending) in one level ($\Delta M = 0, \pm 1$) is equal to the intensity sum of all lines originating (ending) in any other level. In addition to these symmetry and sum rules is the requirement that, viewed in any direction, the radiation summed over all components is unpolarized. Satisfaction of these laws requires that

$$\sum_n \epsilon_n^{(0)} = \frac{1}{2} \quad \sum_n \epsilon_n^{(-1)} = \sum_n \epsilon_n^{(1)} = \frac{1}{4} \quad (42)$$

and the zeroth spectral moment of equation (41) is unchanged from equation (30).

The first spectral moment of the measurement g is readily calculated as

$$\mu^{(1)} = \mu_D^{(1)} + \mu_B^{(1)} \sin \delta \quad (43)$$

with the Doppler component given by equation (31) and the Zeeman component given by

$$\mu_B^{(1)} = \int_{L(p,\phi)} I_0(\mathbf{r}) \beta_B(\mathbf{r}) \cdot d\mathbf{l} \quad (44)$$

$$\beta_B(\mathbf{r}) = \zeta \frac{\mu \mathbf{B}_p(\mathbf{r})}{h\nu_0} \quad (45)$$

$$\zeta = \left(\sum_n w_n^{(1)} \epsilon_n^{(1)} \right) / \left(w_B \sum_n \epsilon_n^{(1)} \right) \quad (46)$$

$$w_B = \mu B / h\nu_0. \quad (47)$$

The factor ζ (of order unity) is the intensity weighted frequency shift, relative to the fractional shift w_B for a simple triplet, of the circularly-polarized components from the unshifted frequency. Note that, although both left and right circular components contribute with equal weight, the first moment is independent of the overall line-shape details of the Zeeman multiplet. Methods that rely on fitting the net circular-polarization spectral profile must normally allow for the multiplet structure [26]. Equation (44) is a longitudinal vector line-integral measurement that could in principle be inverted to give local estimates of the toroidal current density. Doppler and Zeeman shifts can be distinguished by piezoelectric modulation of the phase δ in equation (43). The second spectral moment is calculated in a similar way.

5. Other applications

A number of additional plasma diagnostic applications of vector tomography, both active and passive, come to mind. The most obvious example is, of course, laser polarimetry where both longitudinal and transverse plasma magnetic field components are conveyed by the change in tilt and ellipticity of the electric vector respectively [7, 24]. Another refractivity based technique is Schlieren imaging, or beam-deflection tomography [8]. This diagnostic is sensitive to the transverse gradient of the refractive index along the line-of-sight and has been employed with great success for the study of supersonic flows and flames.

Interferometry and forward angle fluctuation diagnostics (scintillation and phase-contrast interferometry for example) register information about the transverse flow field. These diagnostics operate in the regime $\mathbf{k}_0 \cdot \mathbf{K} \approx 0$, where \mathbf{k}_0 is the incident wavevector and \mathbf{K} is the plasma scattering component. Propagating spatially coherent structures of various scalelengths are manifest as temporal oscillations or fluctuations in the detector signals. The scattered (detected) wave frequency is Doppler shifted by $\omega = \mathbf{K} \cdot \mathbf{v}(\mathbf{r})$ from the incident frequency ω_0 , and this shift is integrated over the line-of-sight. For interferometric schemes (e.g. scintillation interferometry), the spatio-temporal Fourier transform of the phase shift is proportional to [14] (cf equation (26))

$$\tilde{\varphi}(\mathbf{K}, \omega) = \int_{L(p, \phi)} \tilde{n}_e(\mathbf{K}, l) \delta(\omega - \mathbf{K} \cdot \mathbf{v}) dl. \quad (48)$$

When integrated over ω , equation (48) expresses the central slice theorem for tomography of scalar quantities. For measurements made using a one-dimensional detector array oriented in the x -direction (transverse to laser beam propagation in the y -direction), the first temporal frequency moment of $\tilde{\varphi}$ gives the transverse component of \mathbf{v} weighted by the fluctuation spectrum

$$\int_{-\infty}^{\infty} \omega \tilde{\varphi}(K_x, \omega) d\omega = K_x \int_{L(p, \phi)} \tilde{n}_e(K_x; y, z) v_x dy. \quad (49)$$

This is, of course, a transverse vector tomography problem. For Schlieren measurements, the temporal frequency weighting is accomplished naturally through the wavenumber response of the diagnostic.

As a final example, we might consider the tomography of the toroidal magnetic flux using a rotatable array of narrow strip flux loops. Such an experiment could be constructed for study of H-1 plasmas in the low-field, low-temperature (but modest $\beta \sim 0.2\%$) operating regime. Plasma pressure induced toroidal and poloidal currents have been measured to flow under these conditions in H-1 using area-integrating Rogowski loops inserted into the plasma [21]. The apparatus would be fashioned after the already operating rotating wire array used for vacuum e-beam tomography on H-1 [4] and would consist of a parallel array of thin quartz-insulated plasma-immersed wire loops mounted on a rotatable carrier that surrounds the plasma. Measurements of the time-integrated emf generated at the terminals of the loops at many angular positions can be inverted to recover the distribution in the poloidal plane of the toroidal flux (though boundary field components must now be considered). The wire flux loop array would have the capability to map this flux distribution with high spatial resolution for comparison with the predictions of resistive MHD equilibrium codes.

6. Simulations

For these simulations we consider the poloidal flow driven by a hypothetical radially directed electric field in the plasma poloidal cross section. The emission profile is first represented in circular flux coordinates by the simple Gaussian distribution $\exp(-r^2/\Delta r^2)$ of width $\Delta r = 0.5$. The flow is also modelled in circular flux coordinates by constructing scalar potentials W_z and V that simulate the $E_r \times B_T$ vortex and a circularly-symmetric arbitrary velocity sink located at a given flux surface ($r = 0.4$). The circular distributions are warped using a geometric transformation into a bean shape that closely matches the H-1 vacuum surfaces. The warped scalar and vector potential functions are shown in figures 2(a) and 2(c), respectively, and the associated flow fields $\mathbf{E}_V = -\nabla V$ and $\mathbf{E}_W = \nabla \times W_z \hat{\mathbf{k}}$ are presented in figures 2(b) and 2(d).

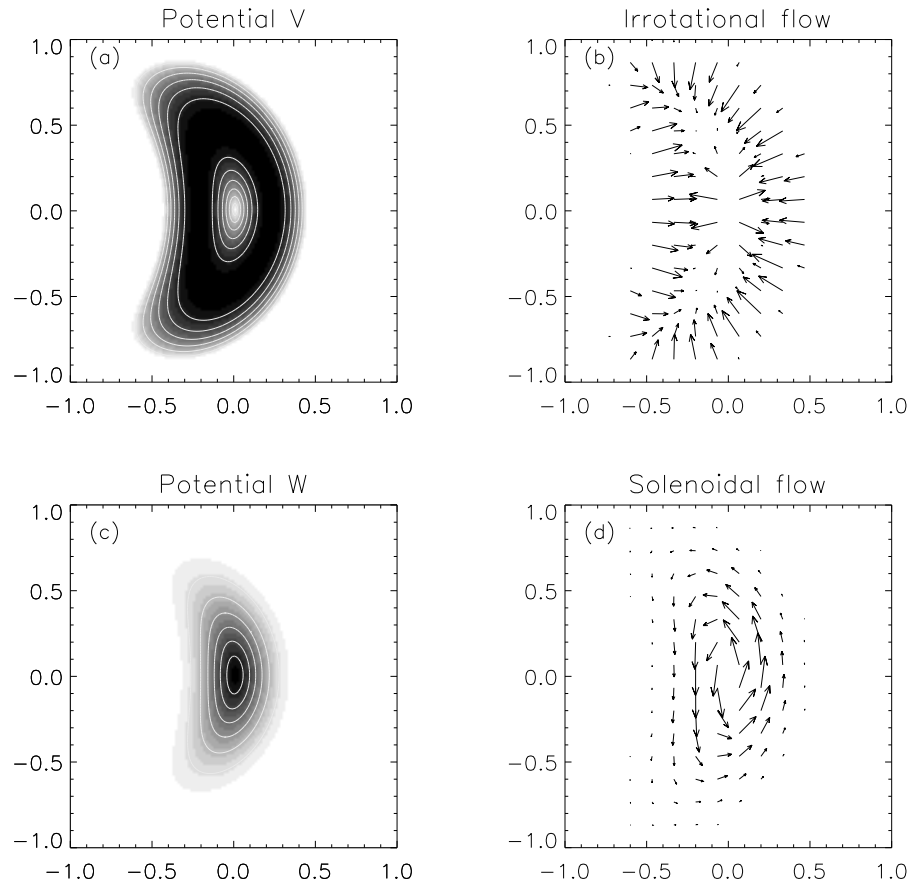


Figure 2. (a), (b) Potential function and associated flow pattern respectively for the irrotational component and (c), (d) the solenoidal part of the model flow field.

For the measurements, we assume a 12 view optical system in the poloidal cross section with each view having 32 equispaced chords. In this simple arrangement, many of the chords do not see the plasma emission, so that the number of effective channels is somewhat less. This large number of channels is not unreasonable given the excellent access to the plasma in H-1 and ready availability of multi-element detector arrays. The low-order spectral moments are computed directly for each of the viewing chords and a k -space filtered back-projection algorithm applied for reconstruction of the various scalar fields (see the appendix). For brevity we do not consider reconstruction of the scalar temperature field. The reconstructions are performed on a cartesian grid with no symmetry, smoothness or positivity constraints. More sophisticated algorithms such as ART or MEM that allow the imposition of *a priori* information would be expected to give superior reconstruction accuracy.

The phantom emission intensity distribution is shown in figure 3(a) and its reconstruction in figure 3(b). The calculated longitudinal ‘sinogram’ $G_l(p, \phi)$ (first moment) is displayed in figure 3(c). The sinogram exhibits both negative and positive values and exhibits the symmetry $G_l(p, \phi) = -G_l(-p, \phi + \pi)$. Figure 3(d) shows the reconstructed vector potential

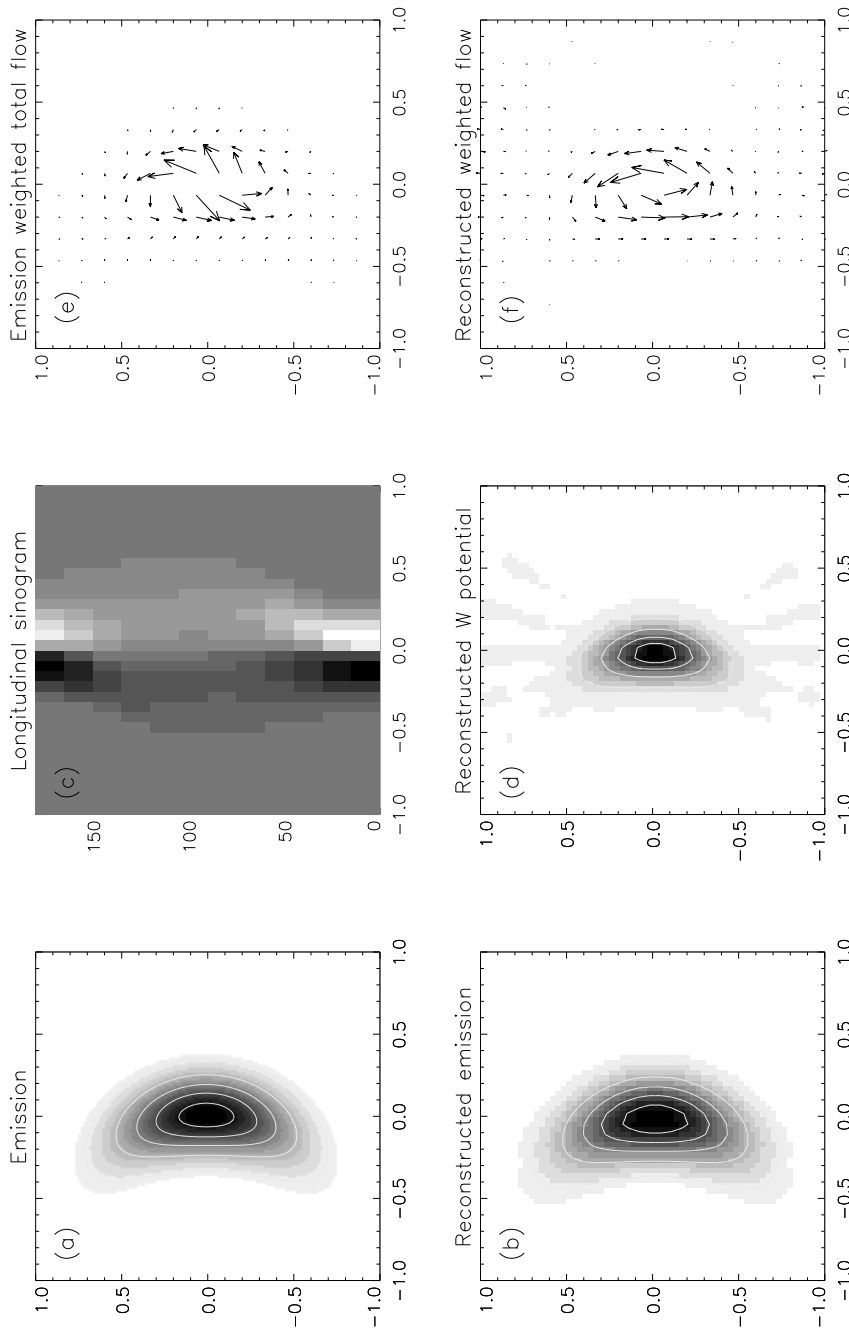


Figure 3. Phantom and reconstructed flow patterns for H-1 vector spectroscopy: (a), (b) the model and reconstructed emission profiles; (c), (d) the longitudinal interaction sinogram $G(p, \phi)$ for the 12 view system and the associated reconstructed potential; (e) the emission-weighted total flow pattern and (g) the emission-weighted solenoidal flow field inferred from the reconstructed potential.

for the emission weighted total flow field $I_0 \mathbf{v}$ while figure 3(e) shows the flow pattern for this field. For comparison, the ‘flow’ pattern associated with the reconstructed potential is given in figure 3(f). Because the conditions expressed by equation (35) are approximately satisfied for this model flow, the reconstructed flow is not influenced by the irrotational component of the total flow field.

Acknowledgments

I wish to thank Dr John Hey for his welcome comments. I am grateful to the Australian Research Council for financial support during this research. The work was completed while on study leave at the FOM-Instituut voor Plasmafysica, ‘Rijnhuizen’ in the Netherlands. I wish to acknowledge support from NWO during this time and express my gratitude to the Institute for their great hospitality during my stay.

Appendix

Since the forms of equations (17) and (18) are identical it will suffice to consider reconstruction in the longitudinal case only. Using equation (17) the longitudinal line integral can be expressed as

$$\begin{aligned} G_l(p, \phi) &= \frac{\partial}{\partial p} \int_{L(p, \phi)} W_z dl \\ &= \iint_R W_z(\mathbf{r}) \delta'(p - \mathbf{r} \cdot \hat{\mathbf{p}}) d\mathbf{r} \end{aligned} \quad (50)$$

where $d\mathbf{r} \equiv dx dy$, R is the region of integration (see figure 1) and we have ignored boundary terms. A first approach to reconstruction would then be to apply standard tomographic algorithms to the integrated quantity

$$I(p, \phi) = \int_{-\infty}^p G_l(p', \phi) dp' = \int_{L(p, \phi)} W_z dl. \quad (51)$$

Alternatively, a back-projection based reconstruction algorithm can be found by taking the inverse Fourier transform of equation (17). In polar coordinates we obtain

$$W_z(\mathbf{r}) = \frac{-i}{(2\pi)^2} \int_0^\pi d\phi \int_{-\infty}^\infty d\kappa \operatorname{sgn}(\kappa) \tilde{G}_l(\kappa, \phi) \exp[i\kappa r \cos(\theta - \phi)]. \quad (52)$$

Substituting for \tilde{G}_l and integrating over κ gives the convolution form

$$W_z(\mathbf{r}) = \frac{-1}{2\pi^2} \int_0^\pi d\phi \int_{-\infty}^\infty dp G_l(p, \phi) H(x \cos \phi + y \sin \phi - p) \quad (53)$$

$$H(p) = \frac{1}{p}. \quad (54)$$

This result was obtained by Braun and Hauck [5] using the inverse Radon transform and also by Faris and Byer [8] in the context of optical Schlieren tomography.

For parallel beam measurements with a sampling interval τ the limits for the rightmost integral in equation (52) become $\pm K = \pi/\tau$. It is assumed that G_l is effectively spatially bandlimited to this maximum wavenumber so that aliasing can be neglected. In the discrete case, the space domain convolving filter becomes

$$H(p) = \frac{\sin^2(Kp/2)}{p}. \quad (55)$$

For this filter and bandlimited G_l , the discretized version of equation (52) is evaluated exactly for measurements at the sample points $p = n\tau$, and offers an efficient means for reconstruction of W_z .

References

- [1] Balandin A, Fuchs G, Pickalov V, Rapp J and Soltwisch H Vector tomography of plasmas using Faraday rotation *Proc. VI Int. Symp. on Computerized Tomography (Novosibirsk, Russia, August 10–14, 1993)*
- [2] Batchelor G K 1987 *An Introduction to Fluid Dynamics* (Cambridge: Cambridge University Press)
- [3] Bell R J 1972 *Introductory Fourier Transform Spectroscopy* (New York: Academic)
- [4] Blackwell B D, Howard J and Tumlos R B 1992 Tomographic wire-grid imaging of magnetic surfaces *Rev. Sci. Instrum.* **63** 4725–7
- [5] Braun H and Hauck A 1991 Tomographic reconstruction of vector fields *IEEE Trans. Sig. Proc.* **39** 464–71
- [6] Candler C 1964 *Atomic Spectra* (London: Hilger and Watts)
- [7] DeMarco F and Segre S E 1972 The polarization of an e.m. wave propagating in a plasma with magnetic shear *Plasma Phys.* **14** 245–52
- [8] Faris G W and Byer R L 1988 Three-dimensional beam-deflection optical tomography of a supersonic jet *Appl. Opt.* **27** 5202–12
- [9] Feldman U, Seeley J F, Sheeley N R Jr, Suckewer S and Title A M 1984 Magnetic field measurements in tokamak plasmas *J. Appl. Phys.* **56** 2512–18
- [10] Fonck R J, Duperrex P A and Paul S F 1990 Plasma fluctuation measurements in tokamaks using beam-plasma interactions *Rev. Sci. Instrum.* **61** 3487–95
- [11] Fonck R J, Goldston R J, Kaita R and Post D E 1983 *Appl. Phys. Lett.* **42** 239
- [12] Hamberger S M, Blackwell B D, Sharp L E and Shenton D B 1990 H-1 design and construction *Fusion Technol.* **17** 123–30
- [13] Howard J 1988 Tomography and reliable information *J. Opt. Soc. Am. A* **5** 999
- [14] Howard J and Sharp L E 1992 Diffraction analysis of forward-angle scattering in plasmas *Plasma Phys. Control. Fusion* **34** 1133–56
- [15] Huang L K *et al* 1990 Safety factor on the axis of a tokamak during ohmically heated sawtooth discharges from a localized measurement of circular polarization of the Li 6708 Å line *Phys. Fluids B* **2** 809–14
- [16] Hutchinson I H 1987 *Principles of Plasma Diagnostics* (Cambridge: Cambridge University Press)
- [17] Ingesson L C, Pickalov V V, Donne A J H, RTP Team and Schram D C 1995 First tomographic reconstructions and a study of interference filters for visible light tomography on RTP *Rev. Sci. Instrum.* **66** 622–4
- [18] Kuramoto H, Hiraki N, Moriyama S, Toi K, Sata K and Narihara K 1995 Measurements of poloidal magnetic field with high time resolution Zeeman polarimeter *Proc. 7th Int. Toki Conf. on Plasma Physics and Controlled Fusion* in press
- [19] Phillips H B 1960 *Vector Analysis* (New York: Wiley)
- [20] Ramsay A T and Turner S L 1987 Haifa: a modular, fiber-optic coupled, spectroscopic diagnostic for plasmas *Rev. Sci. Instrum.* **58** 1211–20
- [21] Shats M, Blackwell B D, Borg G G, Hamberger S M, Howard J, Rudakov D L and Sharp L E 1995 Magnetic configuration scans in H-1 heliac *Fusion Technol.* **27** 286–9
- [22] Shaw R S 1987 Plasma-rotation determination from spectral intensity measurements *J. Opt. Soc. Am. A* **4** 2254–59
- [23] Spanjers G G, Yadlowsky E J, Hazelton R C, Moschella J J and Settersten T B 1995 Zeeman absorption measurements of two-dimensional magnetic field structures *Rev. Sci. Instrum.* **66** 1189–92
- [24] Veron D 1979 Submillimeter interferometry of high density plasmas *Infrared and Millimeter Waves* vol 2, ed K J Button (New York: Academic) pp 69–135
- [25] Winters K B and Rouseff D 1993 Tomographic reconstruction of stratified fluid flow *IEEE Trans. Ultrason., Ferroelectr. Freq. Control* **40** 26–33
- [26] Wroblewski D, Huang L K and Moos H W 1988 Scanning polarimeter for measurement of the poloidal magnetic field in a tokamak *Rev. Sci. Instrum.* **59** 2341–50
- [27] Wroblewski D and Lao L L 1992 Polarimetry of motional stark effect and determination of current profiles in DIII-D *Rev. Sci. Instrum.* **63** 5140–7
- [28] Wroblewski D, Moos H W and Rowan W L 1986 Zeeman effect polarimetry of Ti VXII 3834 Å line in Texas experimental tokamak *Appl. Phys. Lett.* **48** 21–3